

# Field-resolved infrared spectroscopy of biological systems

<https://doi.org/10.1038/s41586-019-1850-7>

Received: 1 February 2019

Accepted: 29 October 2019

Published online: 1 January 2020

Ioachim Pupeza<sup>1,2,5\*</sup>, Marinus Huber<sup>1,2,5</sup>, Michael Trubetskov<sup>2</sup>, Wolfgang Schweinberger<sup>1,3</sup>, Syed A. Hussain<sup>1,2</sup>, Christina Hofer<sup>1,2</sup>, Kilian Fritsch<sup>1</sup>, Markus Poetzlberger<sup>2</sup>, Lenard Vamos<sup>2</sup>, Ernst Fill<sup>1</sup>, Tatiana Amotchkina<sup>1</sup>, Kosmas V. Kepesidis<sup>1</sup>, Alexander Apolonski<sup>1</sup>, Nicholas Karpowicz<sup>2</sup>, Vladimir Pervak<sup>1,2</sup>, Oleg Pronin<sup>1,2</sup>, Frank Fleischmann<sup>2,4</sup>, Abdallah Azzeer<sup>3</sup>, Mihaela Žigman<sup>1,2,4</sup> & Ferenc Krausz<sup>1,2,4\*</sup>

The proper functioning of living systems and physiological phenotypes depends on molecular composition. Yet simultaneous quantitative detection of a wide variety of molecules remains a challenge<sup>1–8</sup>. Here we show how broadband optical coherence opens up opportunities for fingerprinting complex molecular ensembles in their natural environment. Vibrationally excited molecules emit a coherent electric field following few-cycle infrared laser excitation<sup>9–12</sup>, and this field is specific to the sample's molecular composition. Employing electro-optic sampling<sup>10,12–15</sup>, we directly measure this global molecular fingerprint down to field strengths  $10^7$  times weaker than that of the excitation. This enables transillumination of intact living systems with thicknesses of the order of 0.1 millimetres, permitting broadband infrared spectroscopic probing of human cells and plant leaves. In a proof-of-concept analysis of human blood serum, temporal isolation of the infrared electric-field fingerprint from its excitation along with its sampling with attosecond timing precision results in detection sensitivity of submicrograms per millilitre of blood serum and a detectable dynamic range of molecular concentration exceeding  $10^5$ . This technique promises improved molecular sensitivity and molecular coverage for probing complex, real-world biological and medical settings.

The molecular composition of living organisms is a sensitive indicator of their physiological states. Even apparently simple physiological transitions are often connected to highly multivariate concurrent molecular changes. Therefore, the capability to simultaneously observe changes in concentrations of a variety of molecules embedded in complex organic consortia is likely to be instrumental in advancing biology and medical diagnostics systems.

Many biologically relevant changes occur at concentration levels that are often not detectable in system-wide molecular milieus owing to the vast dynamic range of molecular concentrations<sup>1</sup>. Simultaneous quantitative probing of multiple molecules within a complex consortium relies on either biochemical separation of certain types of molecules or depletion of highly abundant ones<sup>16</sup>. Such approaches are time-consuming or expensive or suffer from poor reproducibility, impeding robust, high-throughput implementations. Here we harness broadband optical coherence to address this challenge directly.

Optical spectroscopy of biological samples interrogates the chemical substructures of intact molecules (molecular fragments<sup>17</sup>) rather than molecules as a whole<sup>18,19</sup> by detecting their resonant vibrational response to infrared or Raman excitation. Occurrence of the same or similar fragments in different biomolecules and rapid dephasing results in overlapping temporal and spectral responses and hampers

the identification of individual molecules<sup>2–4</sup> in complex samples. However, the detected superposition of the responses of all fragments is characteristic of molecular composition, representing what may be referred to as the global molecular fingerprint (GMF) of the sample.

Higher excitation power increases the GMF signal, making smaller changes in the sample's molecular composition detectable. In spectroscopies that capture time-integrated fields<sup>11,20–23</sup>—that is, frequency-resolved spectroscopy—the GMF signal hits the detector along with the (much stronger) excitation transmitted through the sample. This has far-reaching implications. First, in the limit of strong excitation, the weakest molecular signal detectable tends to be limited by the technical noise of the excitation source<sup>22,24</sup>. Second, and more fundamentally, even in the absence of technical noise, saturation of the detector (elements) places a limit on the sensitivity<sup>11,22,24</sup>. These limitations are schematically illustrated in Fig. 1a, see 'Frequency-resolved spectroscopy'.

In this work, we show how time-resolved sampling of the electric field emitted by impulsively excited molecular vibrations allows us to overcome these limitations by isolating the retarded molecular signal from any excitation background. We term the technique field-resolved spectroscopy (FRS). Sensitive sampling of the isolated molecular signal generated by a powerful, ultrashort-pulsed infrared source enables broadband transmission spectroscopy of biological systems in their

<sup>1</sup>Ludwig Maximilians University München, Garching, Germany. <sup>2</sup>Max Planck Institute of Quantum Optics, Garching, Germany. <sup>3</sup>King Saud University, Department of Physics and Astronomy, Riyadh, Saudi Arabia. <sup>4</sup>Center for Molecular Fingerprinting, Budapest, Hungary. <sup>5</sup>These authors contributed equally: Ioachim Pupeza, Marinus Huber. \*e-mail: ioachim.pupeza@mpq.mpg.de; krausz@lmu.de

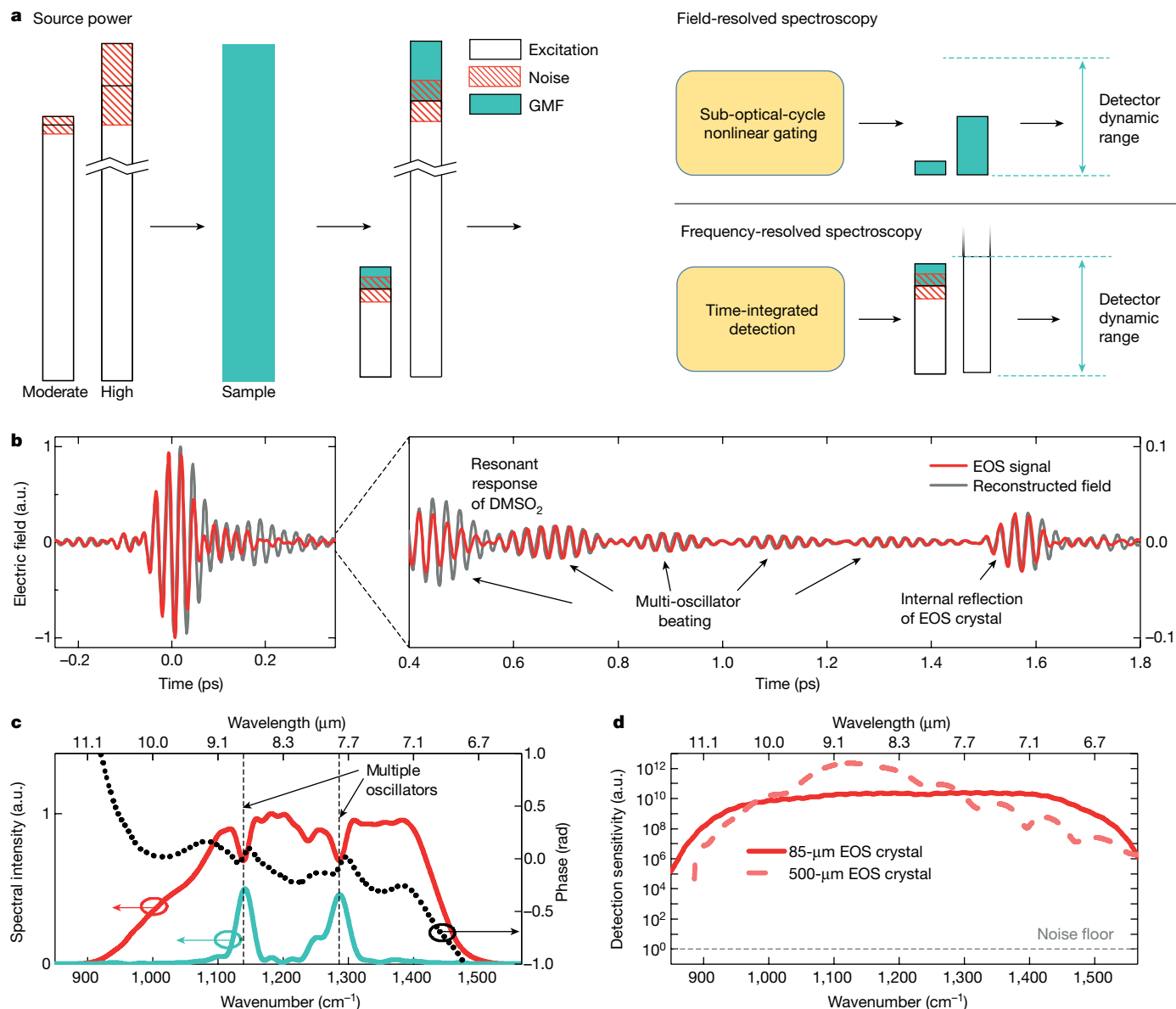


**Fig. 1 | Infrared FRS.** **a**, Schematic comparison of spectroscopic techniques. Infrared light (white bar length indicates source power) with intensity noise (technical noise, red hatching) is transmitted through a sample, acquiring GMF information (cyan shading). For frequency-resolved spectroscopy, the GMF signal is detected ‘on top’ of the excitation signal transmitted through the sample. As a consequence, (1) the GMF signal needs to surpass the excitation noise (surviving balanced detection) and (2) enhancing the GMF signal by increasing the excitation power is limited by the detector’s dynamic range. For FRS, following a few-cycle excitation, sub-optical-cycle nonlinear gating isolates ultrabrief fractions of the GMF from any infrared background, avoiding both requirement (1) and limit (2); see Methods. **b**, Infrared electric field as reconstructed from the measured electro-optic sampling (EOS) trace using an 85- $\mu\text{m}$ -thick GaSe EOS crystal (Supplementary Information section I) after transmission through a solution of 10 mg ml<sup>-1</sup> DMSO<sub>2</sub> in water.

The reconstructed electric field strongly resembles the EOS signal, owing to the broadband instrument response function. The resonant sample response is temporally well separated from the non-resonant response (incorporating the excitation) and exhibits ‘beating’ of several oscillation frequencies. **c**, Fourier transform of the EOS trace shown in **b**, truncated at 1.5 ps to exclude spectral modulations caused by the echo in the EOS crystal. The solid red line shows the spectral intensity, revealing absorption dips associated with vibrational modes of DMSO<sub>2</sub> molecules; the black dashed line shows the spectral phase; the cyan line shows the spectral intensity of the signal in the time window 380–1,500 fs, showing time-filtered GMF information. **d**, Spectral detection sensitivity above the detection noise floor (3-ps time window, 25-s measurement time, transmission through cuvette filled with water). The solid and dashed lines are the bandwidth-optimized versus quantum-efficiency-maximized EOS (Supplementary Information section I), respectively.

natural, aqueous environment (see ‘Field-resolved spectroscopy’ in Fig. 1a).

### Field-resolved molecular spectroscopy

Fourier-transform infrared (FTIR) spectrometers employing thermal radiation sources<sup>20</sup> are the gold standard for broadband vibrational spectroscopy<sup>2–4,7,8,19,24–33</sup>. In liquid samples, they have detected

concentration levels down to several micrograms per millilitre<sup>3,25,27,30,33,34</sup>. This limitation has so far been overcome only by sample drying<sup>33</sup> or targeted detection with functionalized optical biosensors<sup>34,35</sup>.

Recently, tunable quantum cascade lasers<sup>23,24,27,36,37</sup> and femtosecond laser sources<sup>15,38–40</sup> have dramatically enhanced the excitation brilliance. For the reasons sketched in Fig. 1a and explained in the Methods, frequency-resolved spectroscopies have not been able to fully capitalize on this to achieve improved sensitivity and specificity in molecular

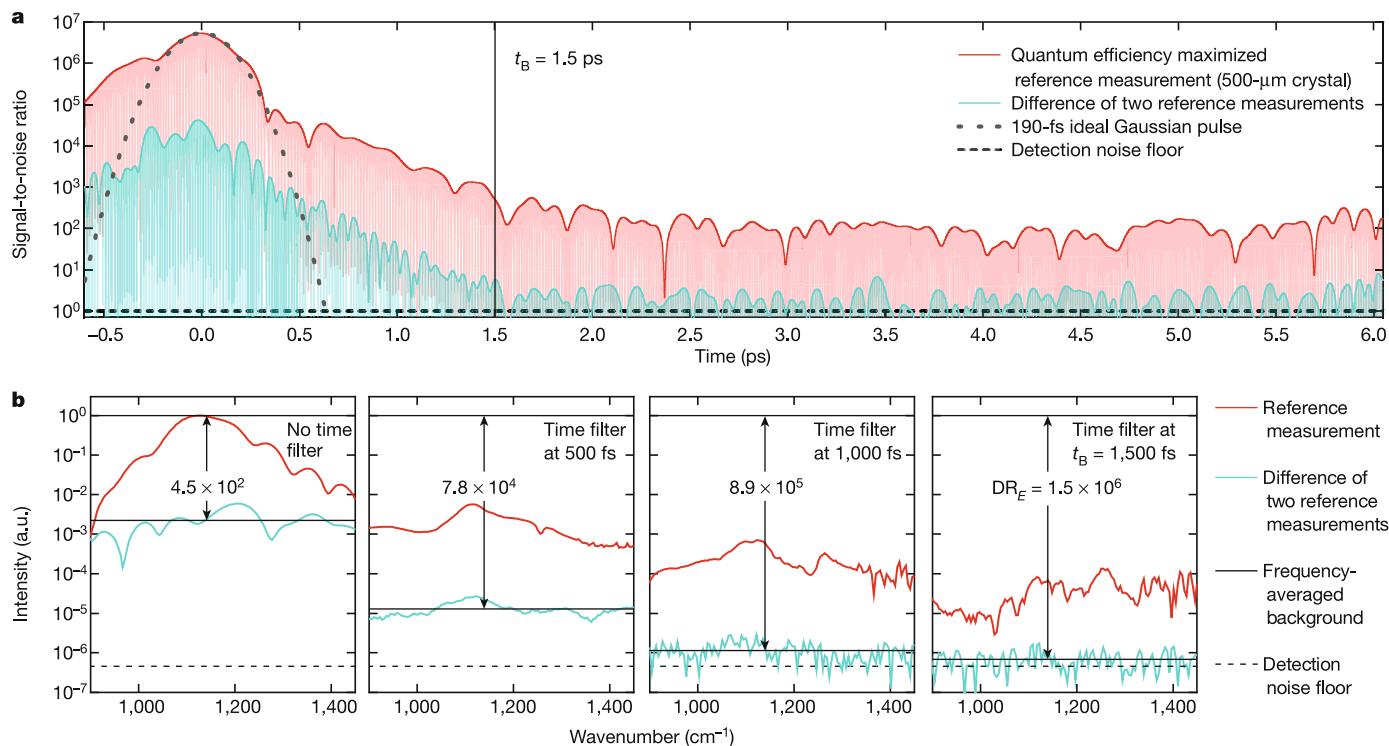


**Fig. 2 | Background quantification for detection of resonant molecular responses.** **a**, The red line is the time-resolved magnitude of the EOS signal (revealing field oscillations) related to the detection noise floor (signal-to-noise ratio), for a reference measurement of pure water (quantum-efficiency-maximized detection setting, 37-s effective measurement time). Following the excitation, the molecular signal from residual atmospheric background in the beam path is observed. The cyan line is the numerical difference of two independent reference measurements. The recorded traces were frequency-

filtered by a 20th-order super-Gaussian filter suppressing any noise outside the spectral window 900–1,450  $\text{cm}^{-1}$ . The grey dotted line is the 190-fs (full-intensity-width-at-half-maximum duration) ideal Gaussian pulse, for comparison. **b**, Frequency-domain definition of  $\text{DR}_E$  and  $t_B$ . The magnitudes of the Fourier transforms of the traces in **a** are shown for different numerical high-pass time filter values. Setting the filter at  $t_B$  (the beginning of the background-free time-domain measurement, rightmost panel) yields an electric-field peak intensity dynamic range of  $\text{DR}_E = 1.5 \times 10^6$  around 1,140  $\text{cm}^{-1}$ .

detection<sup>24,27</sup>. Here, we show how FRS of few-cycle infrared-laser-excited molecular vibrations enables us to take advantage of the temporal structure and power of laser-driven few-cycle infrared sources.

The experimental setup is described in the Methods and in Supplementary Information section I (see also Extended Data Figs. 3, 4). In short, waveform-stable, few-cycle mid-infrared (MIR) pulses abruptly excite molecular vibrations by resonant absorption. The sample-specific electric field (previously referred to as GMF) emitted in the wake of the excitation pulse (Supplementary Video 1 and Methods) is detected via EOS<sup>10,13–15</sup> (Fig. 1b, c). The thickness of the electro-optic crystal controls a trade-off between the bandwidth and the sensitivity of detection (Fig. 1d).

The nonlinear frequency conversion underlying EOS sequentially isolates ultrabrief fractions of the GMF from any infrared background—including the excitation pulse transmitted through the sample, and the thermal background (see Fig. 1a and Methods). Drawing on preliminary experiments<sup>41,42</sup>, here we report a direct measurement of MIR molecular electric fields emanating from biological samples.

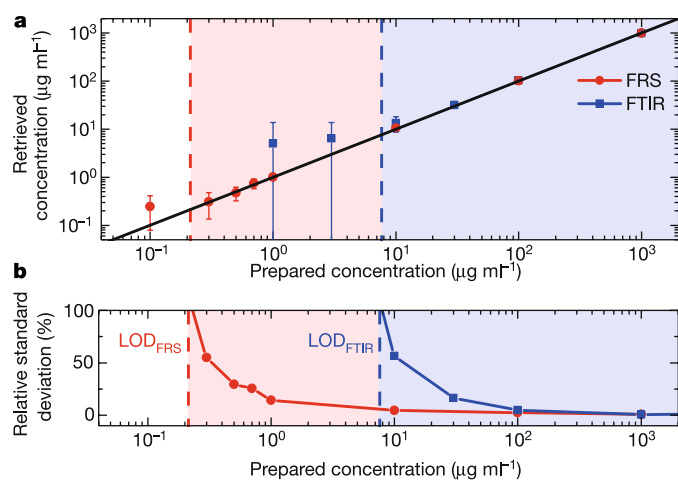


**Fig. 3 | Limit of detection of DMSO2 molecules dissolved in water.** **a**, Results of the concentration retrieval (see Supplementary Information section IV) with quantum-efficiency-optimized FRS (red data points) and FTIR (blue data points). The dots indicate the mean values obtained from at least five measurements per concentration and the error bars show the absolute standard deviation. **b**, Relative standard deviation for the retrieved values. LOD, limit of detection. The coloured shading indicates the range of concentrations exceeding the LOD of each instrument.

### Detection of time-gated molecular signals

In any scheme measuring time-integrated fields, the minimum detectable absorbance,  $\text{MDA}_{\text{FD}}$ , defining the minimum detectable depth of the dips in the red line in Fig. 1c, is given by (Supplementary Information section II):

$$\text{MDA}_{\text{FD}} \approx \sigma \tag{1}$$

where  $\sigma$  represents the relative fluctuations of the measured signal in the considered spectral element. Here,  $\sigma$  incorporates contributions from excitation and detection noise, as well as from the limited detector dynamic range<sup>22</sup>.

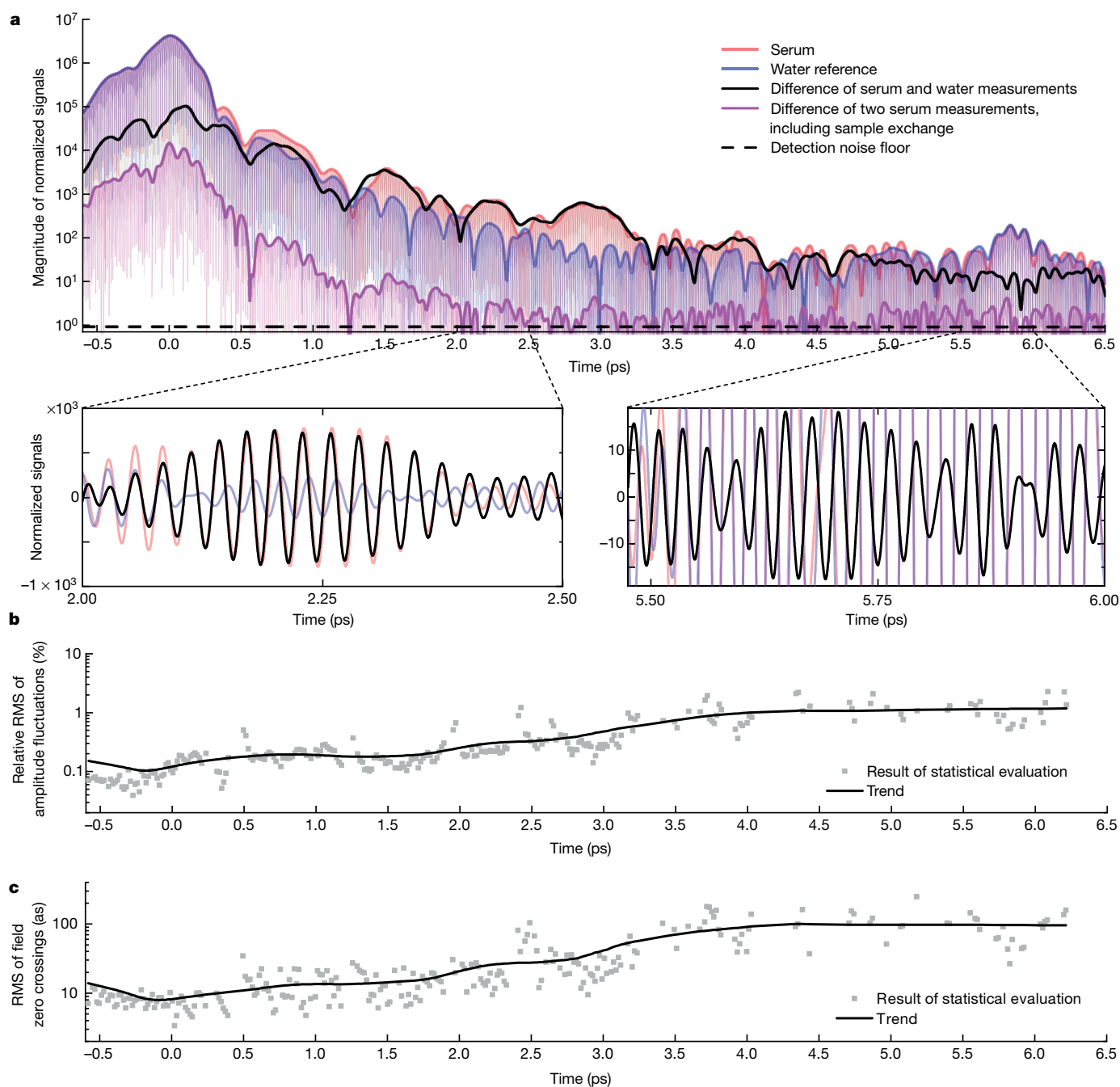


**Fig. 4 | GMFs of human blood serum and their reproducibility. a**, Magnitude of the EOS signals, recorded with quantum-efficiency-optimized FRS (see key). The insets show linear-scale representations of the signals depicted in the main panel in two different time windows. **b, c**, Relative (**b**) and absolute (**c**) root-mean-square (RMS) of oscillation amplitude and zero crossings of five hundred measurements of the GMF of a serum sample (without sample exchange) (see Supplementary Information section V).

In FRS, temporal isolation of (wave-cycle-scale) fractions of the GMF renders the weakest detectable molecular response largely immune against the noise of excitation intensity, as is apparent from the cyan line in Fig. 1c. This is indicated by the expression for the MDA obtained by time-domain modelling of the molecular system with an isolated Lorentzian oscillator of dephasing time  $T_L$  (Supplementary Information section II):

$$\text{MDA}_{\text{FRS}} = \frac{2}{\text{DR}_E} \exp\left(\frac{t_B}{T_L}\right) \quad (2)$$

Here, the dynamic range  $\text{DR}_E$  is defined as the ratio of the spectral amplitude of the electric field of the overall signal reaching the detector at the centre frequency of the Lorentzian oscillator to that of the weakest

signal detectable after passage through a temporal filter opening at  $t_B$ . The parameter  $t_B$  is defined as the instant when the temporal window for an infrared-background-free measurement begins.

This is the case when the numerical difference between two subsequent measurements (in this case, of liquid water) reaches the detection noise floor (Fig. 2a). In our proof-of-principle measurement with the quantum-efficiency-maximized FRS setting, this occurs at about  $t_B = 1,500$  fs, yielding a value of  $\text{DR}_E$  in excess of  $10^6$  for absorptions with centre frequencies between  $1,080 \text{ cm}^{-1}$  and  $1,190 \text{ cm}^{-1}$  (for a 7-ps time window and 37-s effective measurement time, see right panel of Fig. 2b). For a dephasing time of the order of a picosecond, typical for an aqueous environment<sup>9</sup>, equation (2) predicts a minimum detectable absorbance of the order of  $10^{-6}$ .

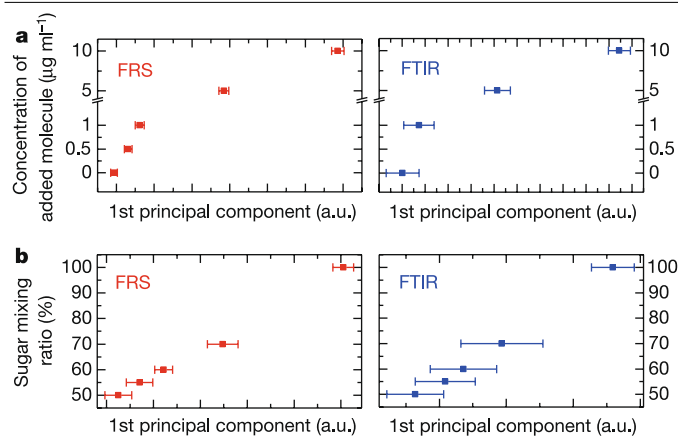


**Fig. 5 | Sensitivity and specificity of FRS of complex fluids performed with bandwidth-optimized sampling.** **a**, Principal component analysis results (separation along the 1st principal component) for a human blood serum sample containing an added aqueous solution of decreasing DMSO<sub>2</sub> concentration, and fingerprinted with FRS using quantum-efficiency-optimized detection (left panel) and with FTIR (right panel). The plots show the mean and relative standard deviation of the values of the 1st principal component for data classes obtained by repeated measurements of samples with nominally identical added DMSO<sub>2</sub> concentration. **b**, Principal component analysis results for a mixture of two sugars dissolved in water with constant total concentration and varying relative concentration (see text), and fingerprinted with FRS using bandwidth-optimized detection (left panel) and with FTIR (right panel).

For experimental verification, we investigated methylsulfonylmethane (DMSO<sub>2</sub>) dissolved in deionized water. FRS was benchmarked against a state-of-the-art FTIR spectrometer equipped with a thermal infrared source (MIRA Analyzer, Micro Biolytics; see Supplementary Information section III). With both instruments, at least five aliquots of concentrations ranging from 1 mg ml<sup>-1</sup> to 100 ng ml<sup>-1</sup> were measured over a duration of  $T = 45$  s each, with a spectral resolution of 4 cm<sup>-1</sup> (realized in FRS by setting the duration of the temporal window of measurement equal to 8.3 ps). Reference measurements of solvent only (deionized water) were performed in alternating order. The concentration values retrieved from the measured data (see Supplementary Information section IV) are summarized in Fig. 3. The limit of detection is defined as the concentration retrieved with a relative standard deviation of 100%. Our study yields an FRS limit of detection of 200 ng ml<sup>-1</sup>, by a factor of 40 lower than that obtained with the FTIR spectrometer (8 μg ml<sup>-1</sup>). This is in agreement with the prediction of equation (2); see Supplementary Information section IV and Extended Data Fig. 7. We estimate a limit of detection of approximately 7 μg ml<sup>-1</sup> for Fourier-transform spectroscopy (FTS)<sup>22</sup> performed with our coherent infrared source and state-of-the-art infrared photodetectors (see Methods).

The exponential dependence of the detection limit on  $\tau_b$  in equation (2) emphasizes how FRS is fundamentally different from any frequency-domain spectroscopy, where  $\tau_b$  is irrelevant (see also Methods). To investigate this dependence—and thereby this hitherto unexplored advantage—we repeated the DMSO<sub>2</sub> dilution series measurement with shorter, sub-60-fs infrared excitation pulses (Supplementary Information section I) and the bandwidth-optimized detection setting of the FRS instrument (Fig. 1d, continuous line). This combination substantially improved the opening time for background-free detection to  $\tau_b = 450$  fs (Supplementary Information section IV). The improvement came at the expense of a factor-of-ten reduction of DR<sub>E</sub> (Fig. 1d). This reduction would, in its own right, result in a factor-of-ten increase of the minimum detectable concentration, according to equation (2). By contrast, we observe an increase from 200 ng ml<sup>-1</sup> to 450 ng ml<sup>-1</sup> only, mainly due to shortening  $\tau_b$  from 1.5 ps to 0.45 ps (Supplementary

Information section IV). This corroborates the predicted sensitivity of MDA<sub>FRS</sub> to  $\tau_b$ .

A more powerful broadband few-cycle infrared source<sup>40</sup> will improve DR<sub>E</sub> while preserving the full bandwidth along with the reduced  $\tau_b$ . This holds promise for a detection limit below 50-ng ml<sup>-1</sup> in combination with super-octave spectral coverage.

### Attosecond-timed molecular signals

For the investigation of complex molecular consortia, the sensitivity and specificity of FRS-based molecular fingerprinting depends critically on the temporal coherence of the GMF signal and its reproducibility over extended measurement time. In gas-phase samples, vibrational dephasing occurs on the nanosecond scale and the required long acquisition delays are advantageously realized with two asynchronous femtosecond oscillators<sup>12,21,43,44</sup>, harnessing optical frequency-comb techniques<sup>45,46</sup>. By contrast, in the liquid phase the coherent molecular signal survives only for several picoseconds<sup>9</sup>. To efficiently use measurement time and ensure attosecond delay precision, we implemented waveform sampling with a mechanical delay line equipped with interferometric delay tracking<sup>47</sup>. Figure 4a shows the field-resolved GMF of a human blood serum sample, as representative of a cell-free bioliquid routinely used in biomedical profiling. The insets in Fig. 4a, b show the differential GMF of the biomolecular ensemble in the sample, as a result of subtracting the signal obtained from pure water from the one of the sample. This ‘pure’ biomolecular signal decays by a few orders of magnitude within 5 ps (compare the left and right panels in Fig. 4b), revealing a dephasing time of collective biomolecular vibrations in human blood serum far below 1 ps.

Five hundred consecutive measurements of the same serum sample yield a relative root-mean-square deviation of the field oscillation amplitude from its mean value of around 0.2% and an absolute root-mean-square of the zero crossings of the infrared GMF field in the range of 20 as, within the first two picoseconds following the excitation (Fig. 4c, d). It is this reproducibility that enables suppression of the electric field background by up to three orders of magnitude via comparison with a reference field (Figs. 2a and 4a), opening the window for background-free measurement less than 2 ps after the excitation pulse peak, even in a highly complex sample such as blood serum (Fig. 4a, magenta line).

### Sensitivity and specificity of FRS

In real-world applications<sup>2–4,26,27</sup>, molecular fingerprinting of complex biofluids will need to probe minuscule changes in the sample’s chemical composition, often caused by low-abundance molecules. The method’s utility for biological or medical applications will be greatly dependent on the smallest changes in molecular concentration that can cause a detectable distortion of the field-resolved GMF. To assess this concentration level, we added controlled amounts of DMSO<sub>2</sub> to the serum sample fingerprinted in Fig. 4a. The results of a principal component analysis of the infrared fingerprints of these samples, measured with our FRS and FTIR devices (Supplementary Information section VI and Extended Data Fig. 8) are shown in Fig. 5a. The plots show the mean and the spread of the data classes of repeated measurements of samples with different concentrations of the added molecule, along the first principal component. FRS appears to clearly separate the sample containing additional DMSO<sub>2</sub> molecules at a concentration of 500 ng ml<sup>-1</sup> from the reference sample. Moreover, the error bars suggest that FRS is capable of detecting changes in molecular concentration down to the 200 ng ml<sup>-1</sup> level in human blood serum, an improvement of nearly an order of magnitude compared to state-of-the-art FTIR spectrometry.

Hence, the smallest changes currently detectable are more than five orders of magnitude below the concentration of the most highly

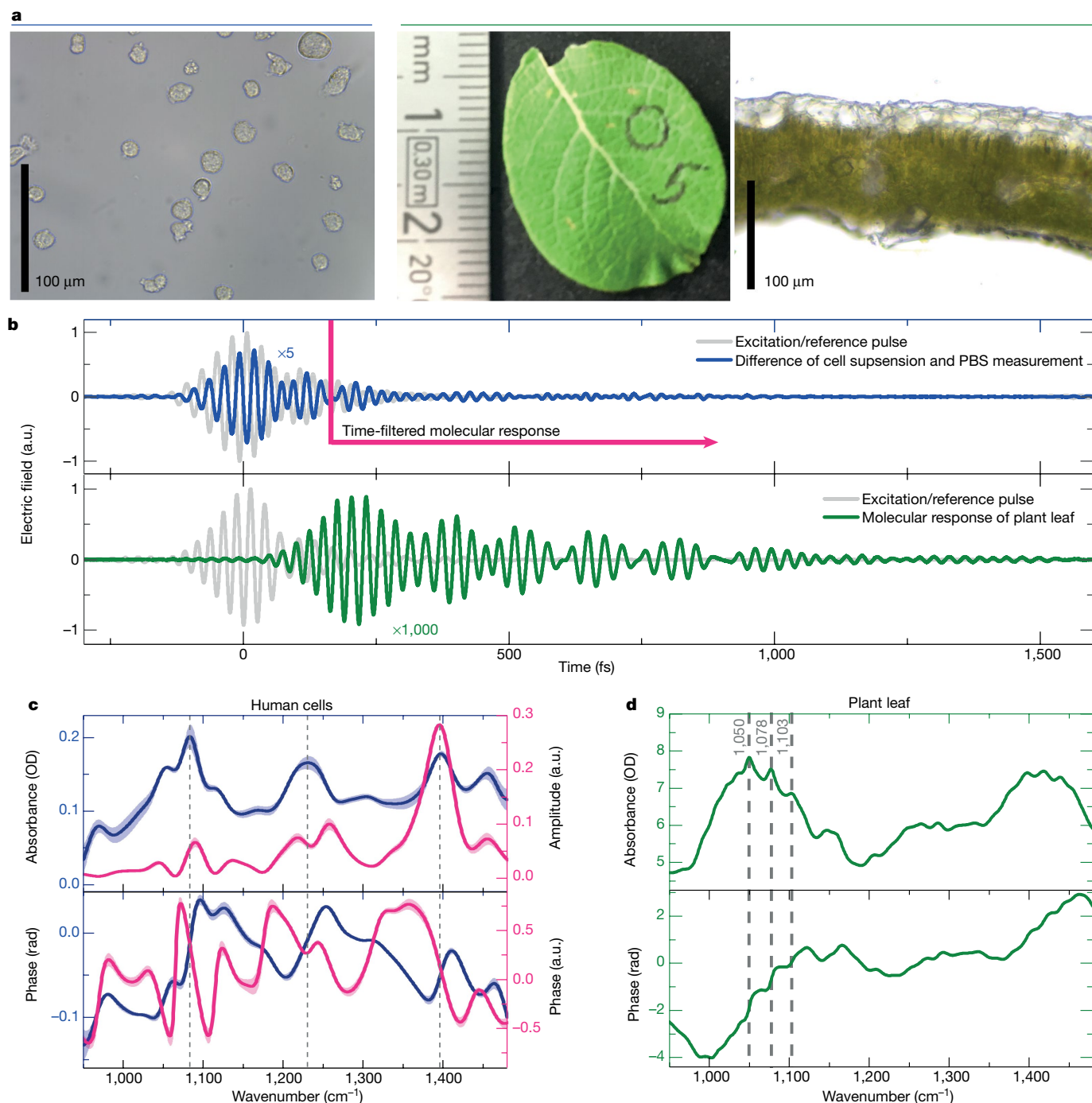


**Fig. 6 | FRS of strongly absorbing living systems.** **a**, The blue-outlined (left) panel is an optical microscope image of cultured human THP-1 cells. The green-outlined panel (right) shows the top and lateral views of a leaf from *Salix caprea*. The measurement of the intact hydrated leaf was performed 5 min after collection, within the marked area. **b**, The upper panel shows GMF of THP-1 cells in suspension, contained in a 100- $\mu\text{m}$ -thick cuvette (blue line) referenced by numerical subtraction to the signal of the suspension medium (phosphate-buffered saline, PBS; grey line). The lower panel shows the molecular response obtained after transmission through a 120- $\mu\text{m}$ -thick leaf of *Salix caprea* (green

line) with air reference (grey line). **c**, Absorption (top panel) and phase (lower panel) spectra of five measurements of human THP-1 cells (blue lines) along with the amplitude and phase of temporally-filtered GMFs (magenta lines). Absorption and phase spectra of the plant leaf are shown in **d**. The standard deviations of multiple measurements in **c** and **d** are indicated by the shaded areas (see Supplementary Information section VII for data processing). We note that the error corridor of the measurement in **d** is smaller than the line thickness and therefore not visible. The grey dotted lines in **c** and **d** indicate prominent absorption peaks.

abundant molecules of blood serum, albumin<sup>1</sup>. This implies a detectable concentration dynamic range in excess of  $10^5$ .

Although the relative intensity noise of the excitation does not affect the FRS limit of molecular detection with a spectrally isolated feature, the lowest detectable concentration of the same molecule in a complex environment is limited by the relative intensity noise of the overall GMF

signal. This, in turn, is likely to be dominated by the noise of the excitation source. As an important consequence, the current FRS concentration dynamic range of  $10^5$  offers substantial room for further improvement by suppressing the noise of the GMF signal. An efficient measure to this end may be ‘freezing’ the excitation source noise by scanning faster than the characteristic time of low-frequency intensity fluctuations<sup>22,48</sup>.

To test the specificity of the measured fingerprints, that is, the sensitivity to small changes in relative concentrations, we prepared aqueous solutions of two different sugar molecules of constant total concentration and varying relative concentrations (Supplementary Information section VI). The total concentration of  $100 \mu\text{g ml}^{-1}$  was chosen to be well above the limit of detection of both instruments. To challenge the method, we used two molecules, maltose and melibiose, which have very similar absorption characteristics (Supplementary Information Section VI and Extended Data Fig. 9). The data in Fig. 5b reveal that FRS outperforms FTIR spectrometry in sensing not only small absolute changes but is also sensitive to relative changes in concentration of molecules of a complex ensemble.

### Probing of intact biological systems

Non-invasive, quantitative probing of intact biological systems would benefit a diversity of biological, biomedical, pharmaceutical and ecological applications. To circumvent sensitivity limitations caused by the strong absorption of infrared radiation in liquid water, so far the majority of studies of biological matter have drawn on sample preparations<sup>7,8,28,29</sup> that substantially alter the state of the sample (such as drying, fixation, slicing, chemical extraction, homogenization and so on). Direct interrogation of intact living systems with infrared spectroscopy has been limited to interaction lengths of the order of  $10 \mu\text{m}$  (or less), either in attenuated-total-reflection geometry<sup>28</sup> or by using extremely thin microfluidic cuvettes<sup>31,32</sup>. Both implementations prevent the majority of living cells from being studied in vivo (for example, human cells are on average larger than  $10 \mu\text{m}$  in diameter). More recently, quantum-cascade lasers have enabled infrared transmission measurements of living systems with path lengths of several tens of micrometres, albeit with restrictions on the bandwidth and with modest signal-to-noise ratios<sup>36,37</sup>.

The unparalleled dynamic range of FRS implemented with a powerful few-cycle infrared source enables these restrictions to be overcome. Here we present the feasibility of infrared fingerprinting of living human cells (THP-1 leukaemic-monocyte-like cell line) cultured and measured directly in suspension (Fig. 6a, left panel) by transillumination of a 0.1-mm-thick flow-through cuvette (see also Supplementary Information section VII). In spite of the order-of-magnitude increase in interaction length as compared to previous broadband measurements of cells from the same cell line<sup>49</sup>, the differential signal originating from the molecules of the cells (blue line in Fig. 6b) is acquired with a high signal-to-noise ratio (Supplementary Information section VII). The corresponding absorption and phase spectra are depicted in Fig. 6c (blue lines), with the former reflecting well the spectral signatures featured by THP-1 cells when squeezed into a  $7\text{-}\mu\text{m}$ -thick cuvette<sup>49</sup>. Temporal gating of the molecular signal (magenta lines in Fig. 6c) uncovers the splitting of the absorption lines at approximately  $1,080 \text{ cm}^{-1}$  and  $1,230 \text{ cm}^{-1}$ , along with relevant phase oscillations—features that are not apparent in the time-integrated spectra (blue lines). This underlines the power of isolating the molecular signal from an (inherently) noisy excitation, offered by FRS.

We have further tested the ability of FRS to acquire transmission spectra of strongly absorbing samples by transilluminating intact plant leaves from the goat willow (*Salix caprea*), a common deciduous tree, with a thickness of approximately  $120 \mu\text{m}$  (Fig. 6a, right panel). The spectra in Fig. 6d feature clearly discernible absorption bands at  $1,050 \text{ cm}^{-1}$ ,  $1,078 \text{ cm}^{-1}$  and  $1,103 \text{ cm}^{-1}$ , corresponding to the C–O stretching motion characteristic of carbohydrates<sup>7,50</sup> widespread in cell walls and cellular compartments of plant leaves. The spectrally resolved attenuation ranges from 5 to 8 orders of magnitude, which is orders of magnitude higher than previously demonstrated in a broadband infrared transmission measurement. In addition, it shows the instrument's ability to resolve absorption over several orders of magnitude in strength without the need to adjust the light power reaching the detector<sup>24</sup>.

### Conclusions and outlook

We have measured infrared-electric-field molecular fingerprints of organic molecules in aqueous solution and in human blood sera. In both settings, the limit of detecting changes in concentration of individual molecules lies in the range of hundreds of nanograms per millilitre for less than one minute of data acquisition time. The amplitude of the coherent emission carrying the GMF of human blood serum was observed to decay by a few orders of magnitude within a few picoseconds. The reproducibility of electric-field oscillations was found to be in the range of tens of attoseconds over a temporal span exceeding six picoseconds following the excitation.

These findings emphasize the performance of FRS of impulsively excited molecular vibrations for GMF of complex biofluids and uncover potential for its further improvement. First, the extremely fast (much less than a picosecond) decay of vibrational coherence in human blood serum suggests an exponential improvement of the detection limit with further steepening of the temporal decay of the excitation transmitted through the sample. Second, the coherence of the recorded molecular signal over spans of several picoseconds along with reduced source-noise-induced GMF noise, by rapid scanning<sup>48</sup>, for example, will increase the detectable range of concentrations in biofluids. The capability of simultaneous probing of multi-molecular changes over a dynamic range of detectable concentration changes in excess of  $10^5$  holds promise for applications in the life sciences and medical diagnostics.

Last, broadband infrared fingerprinting of physiologically relevant living human cells is now feasible in transmission, opening the door for combining infrared fingerprinting with standard flow cytometry. The unparalleled dynamic range of FRS implemented with powerful few-cycle light promises a new regime of transmission-mode vibrational spectroscopy and spectro-microscopy of intact living systems: individual biological cells, bulk-cell and tissue cultures, organs such as plant leaves—all settings in which excessive water absorption has so far constituted a major obstacle.

### Online content

Any methods, additional references, Nature Research reporting summaries, source data, extended data, supplementary information, acknowledgements, peer review information; details of author contributions and competing interests; and statements of data and code availability are available at <https://doi.org/10.1038/s41586-019-1850-7>.

- Geyer, P. E., Holdt, L. M., Teupser, D. & Mann, M. Revisiting biomarker discovery by plasma proteomics. *Mol. Syst. Biol.* **13**, 942 (2017).
- Barth, A. & Haris, P. I. *Biological and Biomedical Infrared Spectroscopy* (IOS Press, 2009).
- Lasch, P. & Kneipp, J. *Biomedical Vibrational Spectroscopy* (Wiley, 2010).
- Baker, M. J. et al. Developing and understanding biofluid vibrational spectroscopy: a critical review. *Chem. Soc. Rev.* **45**, 1803–1818 (2016).
- Hasin, Y., Seldin, M. & Lusis, A. Multi-omics approaches to disease. *Genome Biol.* **18**, 83 (2017).
- Chen, R. et al. Personal omics profiling reveals dynamic molecular and medical phenotypes. *Cell* **148**, 1293–1307 (2012).
- Türker-Kaya, S. & Huck, C. A review of mid-infrared and near-infrared imaging: principles, concepts and applications in plant tissue analysis. *Molecules* **22**, 168 (2017).
- Doherty, J., Cinque, G. & Gardner, P. Single-cell analysis using Fourier transform infrared microspectroscopy. *Appl. Spectrosc. Rev.* **52**, 560–587 (2017).
- Laubereau, A. & Kaiser, W. Vibrational dynamics of liquids and solids investigated by picosecond light pulses. *Rev. Mod. Phys.* **50**, 607–665 (1978).
- Sell, A., Scheu, R., Leitenstorfer, A. & Huber, R. Field-resolved detection of phase-locked infrared transients from a compact Er:fiber system tunable between 55 and 107 THz. *Appl. Phys. Lett.* **93**, 251107 (2008).
- Coddington, I., Swann, W. C. & Newbury, N. R. Time-domain spectroscopy of molecular free-induction decay in the infrared. *Opt. Lett.* **35**, 1395–1397 (2010).
- Kowligy, A. S. et al. Infrared electric field sampled frequency comb spectroscopy. *Sci. Adv.* **5**, eaaw8794 (2019).
- Wu, Q. & Zhang, X.-C. Free-space electro-optic sampling of terahertz beams. *Appl. Phys. Lett.* **67**, 3523–3525 (1995).
- Nahata, A., Weling, A. S. & Heinz, T. F. A wideband coherent terahertz spectroscopy system using optical rectification and electro-optic sampling. *Appl. Phys. Lett.* **69**, 2321–2323 (1996).

15. Pupeza, I. et al. High-power sub-two-cycle mid-infrared pulses at 100 MHz repetition rate. *Nat. Photon.* **9**, 721–724 (2015).
16. Gianazza, E., Miller, I., Palazzolo, L., Parravicini, C. & Eberini, I. With or without you—proteomics with or without major plasma/serum proteins. *J. Proteomics* **140**, 62–80 (2016).
17. Dębska, B. & Guzowska-Świder, B. Fuzzy definition of molecular fragments in chemical structures. *J. Chem. Inf. Comput. Sci.* **40**, 325–329 (2000).
18. Demtröder, W. *Molecular Physics* (Wiley, 2005).
19. Movasaghi, Z., Rehman, S. & ur Rehman, Dr. I. Fourier transform infrared (FTIR) spectroscopy of biological tissues. *Appl. Spectrosc. Rev.* **43**, 134–179 (2008).
20. Griffiths, P. R. & De Haseth, J. A. *Fourier Transform Infrared Spectrometry* (Wiley, 2007).
21. Keilmann, F., Gohle, C. & Holzwarth, R. Time-domain mid-infrared frequency-comb spectrometer. *Opt. Lett.* **29**, 1542–1544 (2004).
22. Newbury, N. R., Coddington, I. & Swann, W. Sensitivity of coherent dual-comb spectroscopy. *Opt. Express* **18**, 7929–7945 (2010).
23. Villares, G., Hugi, A., Blaser, S. & Faist, J. Dual-comb spectroscopy based on quantum-cascade-laser frequency combs. *Nat. Commun.* **5**, 5192 (2014).
24. Schwaighofer, A. et al. Beyond Fourier transform infrared spectroscopy: external cavity quantum cascade laser-based mid-infrared transmission spectroscopy of proteins in the amide I and amide II region. *Anal. Chem.* **90**, 7072–7079 (2018).
25. Haas, J., Catalán, E. V., Piron, P., Karlsson, M. & Mizaikoff, B. Infrared spectroscopy based on broadly tunable quantum cascade lasers and polycrystalline diamond waveguides. *Analyst* **143**, 5112–5119 (2018).
26. Ollesch, J. et al. An infrared spectroscopic blood test for non-small cell lung carcinoma and subtyping into pulmonary squamous cell carcinoma or adenocarcinoma. *Biomed. Spectrosc. Imaging* **5**, 129–144 (2016).
27. Brandstetter, M., Volgger, L., Genner, A., Jungbauer, C. & Lendl, B. Direct determination of glucose, lactate and triglycerides in blood serum by a tunable quantum cascade laser-based mid-IR sensor. *Appl. Phys. B* **110**, 233–239 (2013).
28. Baker, M. J. et al. Using Fourier transform IR spectroscopy to analyze biological materials. *Nat. Protocols* **9**, 1771–1791 (2014).
29. Martin, M. C. et al. 3D spectral imaging with synchrotron Fourier transform infrared spectro-microtomography. *Nat. Methods* **10**, 861–864 (2013).
30. Rohleder, D. et al. Comparison of mid-infrared and Raman spectroscopy in the quantitative analysis of serum. *J. Biomed. Opt.* **10**, 031108 (2005).
31. Bhargava, R. Infrared spectroscopic imaging: the next generation. *Appl. Spectrosc.* **66**, 1091–1120 (2012).
32. Quaroni, L., Zlateva, T., Wehbe, K. & Cinque, G. Infrared imaging of small molecules in living cells: from *in vitro* metabolic analysis to cytopathology. *Faraday Discuss.* **187**, 259–271 (2016).
33. Bonnier, F. et al. Ultra-filtration of human serum for improved quantitative analysis of low molecular weight biomarkers using ATR-IR spectroscopy. *Analyst* **142**, 1285–1298 (2017).
34. Haas, J. & Mizaikoff, B. Advances in mid-infrared spectroscopy for chemical analysis. *Annu. Rev. Anal. Chem.* **9**, 45–68 (2016).
35. Lu, R. et al. High-sensitivity infrared attenuated total reflectance sensors for in situ multicomponent detection of volatile organic compounds in water. *Nat. Protocols* **11**, 377–386 (2016).
36. Haase, K., Kröger-Lui, N., Pucci, A., Schönhals, A. & Petrich, W. Advancements in quantum cascade laser-based infrared microscopy of aqueous media. *Faraday Discuss.* **187**, 119–134 (2016).
37. Haase, K., Kröger-Lui, N., Pucci, A., Schönhals, A. & Petrich, W. Real-time mid-infrared imaging of living microorganisms. *J. Biophoton.* **9**, 61–66 (2016).
38. Gaida, C. et al. Watt-scale super-octave mid-infrared intrapulse difference frequency generation. *Light Sci. Appl.* **7**, 94 (2018).
39. Seidel, M. et al. Multi-watt, multi-octave, mid-infrared femtosecond source. *Science Advances* **4**, eaaq1526 (2018).
40. Butler, T. P. et al. Watt-scale 50-MHz source of single-cycle waveform-stable pulses in the molecular fingerprint region. *Opt. Lett.* **44**, 1730–1733 (2019).
41. Pupeza, I. et al. Field-resolved spectroscopy in the molecular fingerprint region. In *Lasers and Electro-Optics Europe & European Quantum Electronics Conf. (CLEO/Europe-EQEC)* <https://doi.org/10.1109/CLEOE-EQEC.2017.8086859> (IEEE, 2017).
42. Huber, M. et al. Detection sensitivity of field-resolved spectroscopy in the molecular fingerprint region. In *Lasers and Electro-Optics Europe & European Quantum Electronics Conference (CLEO/Europe-EQEC)* <https://doi.org/10.1109/CLEOE-EQEC.2017.8086921> (IEEE, 2017).
43. Timmers, H. et al. Molecular fingerprinting with bright, broadband infrared frequency combs. *Optica* **5**, 727–732 (2018).
44. Muraviev, A. V., Smolski, V. O., Loparo, Z. E. & Vodopyanov, K. L. Massively parallel sensing of trace molecules and their isotopologues with broadband subharmonic mid-infrared frequency combs. *Nat. Photon.* **12**, 209–214 (2018).
45. Udem, T., Holzwarth, R. & Hänsch, T. W. Optical frequency metrology. *Nature* **416**, 233–237 (2002).
46. Ye, J. & Cundiff, S. T. *Femtosecond Optical Frequency Comb: Principle, Operation, And Applications* (Springer, 2005).
47. Schweinberger, W. et al. Interferometric delay tracking for low-noise Mach-Zehnder-type scanning measurements. *Opt. Express* **27**, 4789–4798 (2019).
48. Schubert, O. et al. Rapid-scan acousto-optical delay line with 34 kHz scan rate and 15 as precision. *Opt. Lett.* **38**, 2907–2910 (2013).
49. Birarda, G. et al. IR-Live: fabrication of a low-cost plastic microfluidic device for infrared spectromicroscopy of living cells. *Lab Chip* **16**, 1644–1651 (2016).
50. Max, J.-J. & Chapados, C. Glucose and fructose hydrates in aqueous solution by IR spectroscopy. *J. Phys. Chem. A* **111**, 2679–2689 (2007).

**Publisher's note** Springer Nature remains neutral with regard to jurisdictional claims in published maps and institutional affiliations.

© The Author(s), under exclusive licence to Springer Nature Limited 2019

### Nonlinear time-domain gating in FRS

Here, we elucidate the qualitative differences between FRS and traditional, frequency-resolved spectroscopy. For the latter, we choose FTS as the perhaps most advanced form of frequency-resolved infrared spectroscopy, in particular in the dual-frequency-comb implementation<sup>11,21,22</sup>. Furthermore, the interferograms obtained by FTS performed either with ultrashort pulses<sup>11,21,22</sup> or with broadband, incoherent light<sup>51</sup> resemble the electric field emerging from a sample after resonant excitation with a few-cycle infrared pulse, which FRS samples with sub-optical-cycle resolution by means of nonlinear optics (see Fig. 1b). To understand the important performance differences between the two techniques, it is essential to recognize the conceptual differences in the acquisition of these time-domain signals. First, using simple formalisms for the signals acquired in FTS and FRS, we reveal two major advantages introduced by the time-domain, nonlinear-conversion-based gating of the sampled electric field in FRS over FTS: the robustness of detection sensitivity against technical noise of the MIR excitation transmitted through the sample, and the mitigation or circumvention of the detector-dynamic-range limitation of sensitivity inherent to FTS<sup>22</sup>. Then, we evaluate the performance of FTS achievable with our coherent infrared source and state-of-the-art infrared detection (both described in Supplementary Information section I), employing a well established frequency-domain formalism<sup>22</sup>. Contrasting the results with those of FRS presented in this work, we observe detection sensitivities higher by more than a factor of 30 for FRS of impulsively excited molecular signals decaying with a time constant on the order of 1 ps, as is typical for liquid-phase samples—owing to the above-mentioned advantages.

Extended Data Fig. 1a illustrates the working principle of FTS. Here, we consider an ultrashort-pulsed MIR excitation source. Its broadband pulses are sent along two arms of an interferometer, one of which contains the sample and one of which acts as a ‘local oscillator’ for homodyne (or heterodyne) detection. The field transmitted through the sample is the convolution of the sample response with the incident excitation field<sup>22</sup>  $E_{\text{ex}}(t)$ . It can be written as the sum of (1) a non-resonant response representing an attenuated (and temporally altered) version of  $E_{\text{ex}}(t)$ , which for simplicity we approximate here as  $aE_{\text{ex}}(t)$ , with a scalar  $a < 1$ , and (2) the response  $E_{\text{GMF}}(t)$  of the resonantly excited molecules (a more rigorous treatment of the sample response is given in Supplementary Information section II). The field  $R_{\text{LO}}(t-\tau)$  in the local oscillator arm is a copy of  $E_{\text{ex}}(t)$ , delayed by a variable time  $\tau$ . FRS implemented with EOS (Extended Data Fig. 1b) employs a near-infrared (NIR) gate pulse  $E_{\text{g}}(t-\tau)$  fulfilling two functions<sup>52</sup> (see also Supplementary Information section I). First, this pulse ‘carves out’ an ultrashort portion of the sample response, for instance via a second-order nonlinear upconversion process. Second, it acts as a local oscillator in the homodyne/heterodyne detection of this upconverted signal.

In both schemes, at each delay  $\tau$ , the superposition of the sample response (time-gated and upconverted in the case of FRS) and local oscillator fields is sent to (usually two)  $t$ -integrating intensity detectors placed at each of the sum and difference ports of the beam combiner. In the wake of the excitation, where the strength of  $aE_{\text{ex}}(t)$  can be neglected against that of  $E_{\text{GMF}}(t)$ , the resulting signals recorded by the two respective detectors read:

$$I_{\text{FTS},1,2}(\tau) \propto \int [aE_{\text{ex}}(t) + E_{\text{GMF}}(t)]^2 dt + \int E_{\text{LO}}^2(t-\tau) dt \pm 2 \int E_{\text{GMF}}(t)E_{\text{LO}}(t-\tau) dt \quad (1a)$$

$$I_{\text{FRS},1,2}(\tau) \propto \int [\chi E_{\text{g}}(t-\tau)E_{\text{GMF}}(t)]^2 dt + \int E_{\text{g}}^2(t-\tau) dt \pm 2 \int \chi E_{\text{GMF}}(t)E_{\text{g}}^2(t-\tau) dt \quad (1b)$$

where  $\chi E_{\text{g}}(t-\tau)E_{\text{GMF}}(t)$  is a qualitative expression for the time-gated, upconverted sample response in FRS, neglecting effects such as phase matching or depletion/saturation. The first two right-hand-side terms of equation (1a, b) represent a background (direct-current baseline) around which the third term, containing the spectroscopic information, oscillates. A major difference stems from the first background term in the two equations and immediately becomes apparent after two approximations. In equation (1a), this term can be approximated by  $\int [aE_{\text{ex}}(t)]^2 dt$ , which is typically orders of magnitude larger than the (time-integrated) GMF signal. In equation (1b), owing to temporal gating, the first right-hand-side term is orders of magnitude smaller than the other two terms (see Extended Data Fig. 1c), and can be neglected. With these two approximations, equation (1a, b) becomes:

$$I_{\text{FTS},1,2}(\tau) \propto \int [aE_{\text{ex}}(t)]^2 dt + \int E_{\text{LO}}^2(t-\tau) dt \pm 2 \int E_{\text{GMF}}(t)E_{\text{LO}}(t-\tau) dt \quad (2a)$$

$$I_{\text{FRS},1,2}(\tau) \propto \int E_{\text{g}}^2(t-\tau) dt \pm 2 \int \chi E_{\text{GMF}}(t)E_{\text{g}}^2(t-\tau) dt \quad (2b)$$

The fact that in FTS the time-integrated excitation transmitted through the sample always impinges on the detector(s), whereas in FRS this background term is negligible in the wake of an impulsive excitation, illustrated by equation (2a, b), has two far-reaching implications, described as follows.

**Robustness of FRS against excitation noise.** Although for both schemes the contribution of the local-oscillator term to the background can be readily reduced to the shot-noise/detector-noise level, for example, via lock-in detection (see Supplementary Information section I), in FTS the minimum detectable molecular signal is directly affected by the technical noise of the MIR excitation, whose contribution to the recorded signal is constant along the entire delay range. This requires its suppression by sophisticated fast scanning methods<sup>22</sup> and/or balancing techniques<sup>53,54</sup>. In spite of all these efforts, photon quantum-noise-limited sensitivity<sup>54</sup> has not been experimentally demonstrated for broadband measurements for wavenumbers shorter than 2,000  $\text{cm}^{-1}$ , to the best of our knowledge. In FRS, by contrast, excitation-background-free detection of the molecular signal in the wake of an impulsive excitation implies a sensitivity that is ultimately limited by the quantum noise of the NIR gating field but largely immune to the noise of the MIR excitation.

**Circumvention or mitigation of detector-dynamic-range-induced sensitivity limitation.** In FTS, the usable input power is restricted by the excitation, transmitted through the sample, saturating the detector(s); see the first right-hand-side term of equation (2a). This implies a severe detector-dynamic-range-induced sensitivity limit<sup>11,22</sup> that can only be circumvented/mitigated by techniques such as spectral multiplexing<sup>22</sup> or building the difference between a sample and a reference response to the same excitation interferometrically, before detection<sup>55,56</sup>. This adds substantial complexity to any detection scheme and has not been widely used so far. In FRS, for a fixed local-oscillator power (set to be below the detector saturation level), the signal-to-noise ratio can readily be increased by increasing the excitation field, which linearly increases the sought-for molecular signal  $E_{\text{GMF}}(t)$  in the third right-hand-side term in equation (2b). Because the excitation signal transmitted through the sample is eliminated by the femtosecond temporal gate, the molecular signal can, in principle, be increased up to levels at which  $aE_{\text{ex}}(t)$  vastly exceeds the saturation level of any available detector.

### Sensitivity estimation of FTS implemented with our infrared source

Here, we calculate the expected sensitivity for an FTS implementation employing our infrared radiation source and state-of-the-art MIR

detectors. Because of the delay-independent contribution of excitation noise to the recorded signal (see above), time-domain filtering of the recorded signal does not have such a dramatic effect as in FRS, and well established frequency-domain models for FTS lend themselves for a sensitivity estimation. Here we use the model of Newbury et al.<sup>22</sup> who derived an expression for the frequency-domain signal-to-noise ratio in dependence of detector noise, shot noise, excess laser relative intensity noise (RIN) and detector dynamic range. Although the formula was derived for dual-comb spectroscopy, it can be readily applied to FTS with (slow) mechanical scan, with our experimental parameters (see Supplementary Information section I, Extended Data Fig. 5 and summary in Extended Data Table 1). In addition, we assume no limitations due to digitization, no sequential or parallel multiplexed acquisition and a duty cycle of 1. The power level in both the signal and the local oscillator arms was set to 0.45 mW, limited by detector saturation and well within the range of our source.

For direct comparison with our FRS results, we consider the absorption of DMSO<sub>2</sub> solved in water, spectrally centred at 1,139 cm<sup>-1</sup> (see Extended Data Fig. 6 and parameters in Extended Data Table 1). According to equation (4) of ref.<sup>22</sup>, for these parameters we obtain a limit of detection of 7 µg ml<sup>-1</sup> of DMSO<sub>2</sub> dissolved in water for FTS, which is a factor of 35 above what is demonstrated here with FRS.

### Experimental setup

The instrument (see also Supplementary Information section I for a detailed description) is based on a Kerr-lens mode-locked thin-disk Yb:YAG oscillator<sup>57</sup> emitting a 28-MHz repetition-rate train of 220-fs pulses, spectrally centred at 1,030 nm. After temporal compression via nonlinear spectral broadening based on multi-pass self-phase modulation in bulk fused silica followed by chirped-mirror compressors<sup>58</sup>, the resulting NIR pulses are 16 fs long, with an average power of 60 W. These pulses drive intrapulse difference-frequency generation (optical rectification) in a 1-mm-thick LiGaS<sub>2</sub> crystal. The emerging MIR radiation with an average power of the order of 100 mW is spectrally tunable with a coverage of nearly one octave around a central frequency of 1,200 cm<sup>-1</sup>. After the crystal, the NIR pulse is recycled and used for gating in the EOS detection of the MIR waveforms. Balanced detection in EOS is optimized close to the NIR shot-noise limit, with an impinging NIR power on the GaSe EOS crystal of 420 mW. In order to reduce phase artefacts introduced by variations of the mutual delay between the MIR sampled wave and the NIR sampling pulse, we track this delay interferometrically, with an additional continuous-wave laser<sup>47</sup>. In this manner, data can be recorded with few-nanometre delay precision and a temporal duty cycle close to 100% during forward as well as backward scans. Starting with the last NIR pulse compression stage, all the beams are enclosed in vacuum chambers at a background pressure in the 1-mbar range. Further measures of stabilization include an acousto-optical-modulator-based active noise eater<sup>59</sup> and lock-in detection employing mechanical chopping of the MIR beam.

### Dynamic range of FRS

The 500-µm-thick GaSe electro-optic crystal constitutes a trade-off between a high quantum efficiency and broad bandwidth (Fig. 1d). In addition, it avoids internal reflections within the measurement time window. This quantum-efficiency-optimized apparatus resulted in a linearity of the instrument response over more than seven orders of magnitude of electric-field strength and, moreover, the intensity dynamic range scales linearly with measurement time (Extended Data Fig. 2). Thus, sampling of the oscillating electric field rather than its cycle-averaged intensity<sup>60</sup> results in an unprecedented linear-response intensity dynamic range of >10<sup>14</sup>, vastly exceeding that of infrared spectroscopy so far, to our knowledge<sup>2</sup>. This enables transillumination of aqueous samples of several tens of micrometres in thickness while maintaining a high signal-to-noise ratio.

### Measurement principle and the nature of the signal

FRS molecular fingerprinting relies on the generation of ultrashort infrared pulses with identically repeating electric-field waveforms (in our setup, 28 million such pulses per second). These pulses are transmitted through the sample under investigation, and the waveforms emerging from this interaction are recorded with EOS (see Supplementary Information section I). The spatial distribution of microscopic electric charges (that is, electrons and nuclei) in organic molecules is (1) inhomogeneous and (2) characteristic of the molecular species. Because of (1), when the electric field of the above-mentioned infrared pulses interacts with the molecules, it induces microscopic spatial charge separations (due to the existence of electric dipole moments). These charge separations evolve in time, driven by the oscillating electric field. Because of (2), these microscopic charge oscillations occur with characteristic magnitudes and frequencies—albeit having a fixed mutual timing, set by the common excitation field. In particular, resonant vibrations oscillate long after the excitation by the few-cycle infrared waveform, emanating a GMF. This resonant response is the coherent superposition of the fields of all sample-specific oscillations, thus containing most of the sample-specific information. Importantly, at the centre frequency of any such oscillation, the emission of light as a consequence of the resonant excitation by a light field occurs with opposing phase to the latter<sup>9</sup>. Consequently, the coherent superposition of the GMF and the excitation transmitted through the sample results in a destructive interference at these frequencies, leading to the typical ‘absorption dips’ observed in frequency-domain spectroscopy; see Fig. 1c.

### Data availability

The data that support the findings of this study are available from the corresponding author upon reasonable request.

51. Tsurumachi, N., Fujii, T., Kawato, S., Hattori, T. & Nakatsuka, H. Interferometric observation of femtosecond free induction decay. *Opt. Lett.* **19**, 1867–1869 (1994).
52. Gallot, G. & Grischkowsky, D. Electro-optic detection of terahertz radiation. *J. Opt. Soc. Am. B* **16**, 1204–1212 (1999).
53. Hobbs, P. C. D. Ultrasensitive laser measurements without tears. *Appl. Opt.* **36**, 903–920 (1997).
54. Foltynowicz, A., Ban, T., Mastowski, P., Adler, F. & Ye, J. Quantum-noise-limited optical frequency comb spectroscopy. *Phys. Rev. Lett.* **107**, 233002 (2011).
55. Buberl, T. Broadband interferometric subtraction of optical fields. *Opt. Express* **27**, 2432–2443 (2019).
56. Tomberg, T., Muraviev, A., Ru, Q. & Vodopyanov, K. L. Background-free broadband absorption spectroscopy based on interferometric suppression with a sign-inverted waveform. *Optica* **6**, 147–151 (2019).
57. Fritsch, K., Poetzlberger, M., Pervak, V., Brons, J. & Pronin, O. All-solid-state multipass spectral broadening to sub-20 fs. *Opt. Lett.* **43**, 4643–4646 (2018).
58. Schulte, J., Sartorius, T., Weitenberg, J., Vernaleken, A. & Russbueldt, P. Nonlinear pulse compression in a multi-pass cell. *Opt. Lett.* **41**, 4511–4514 (2016).
59. Huber, M. et al. Active intensity noise suppression for a broadband mid-infrared laser source. *Opt. Express* **25**, 22499–22509 (2017).
60. Lanin, A. A., Voronin, A. A., Fedotov, A. B. & Zheltikov, A. M. Time-domain spectroscopy in the mid-infrared. *Sci. Rep.* **4**, 1–8 (2014).

**Acknowledgements** We thank D. Gerz, A. Zigman Kohlmaier, L. Fuerst and I. Kosse for their contributions and help with the measurements. We acknowledge the support of the Max Planck Society, the Center for Advanced Laser Applications of the Ludwig-Maximilians University and the King Saud University via the Researchers Supporting Project (NSRSP-2019/1).

**Author contributions** I.P., M.H., M.T., W.S., S.A.H., C.H., E.F., A. Apolonski, A. Azzeer, M.Z. and F.K. conceived the experiments. I.P., M.H., M.T., W.S., S.A.H., C.H., K.F., M.P., L.V., T.A., K.V.K., N.K., V.P., O.P., M.Z. and F.K. designed the experiments and analysed the experimental data. M.H., F.F. and M.Z. prepared the living systems. S.A.H., K.F., M.P. and O.P. designed and built the few-cycle near-infrared femtosecond laser source. I.P., M.H., W.S., S.A.H., C.H., L.V., V. P. and N.K. developed the optical system for the generation and electro-optic detection of waveform-stable MIR radiation. All authors contributed to evaluating the results and writing the manuscript.

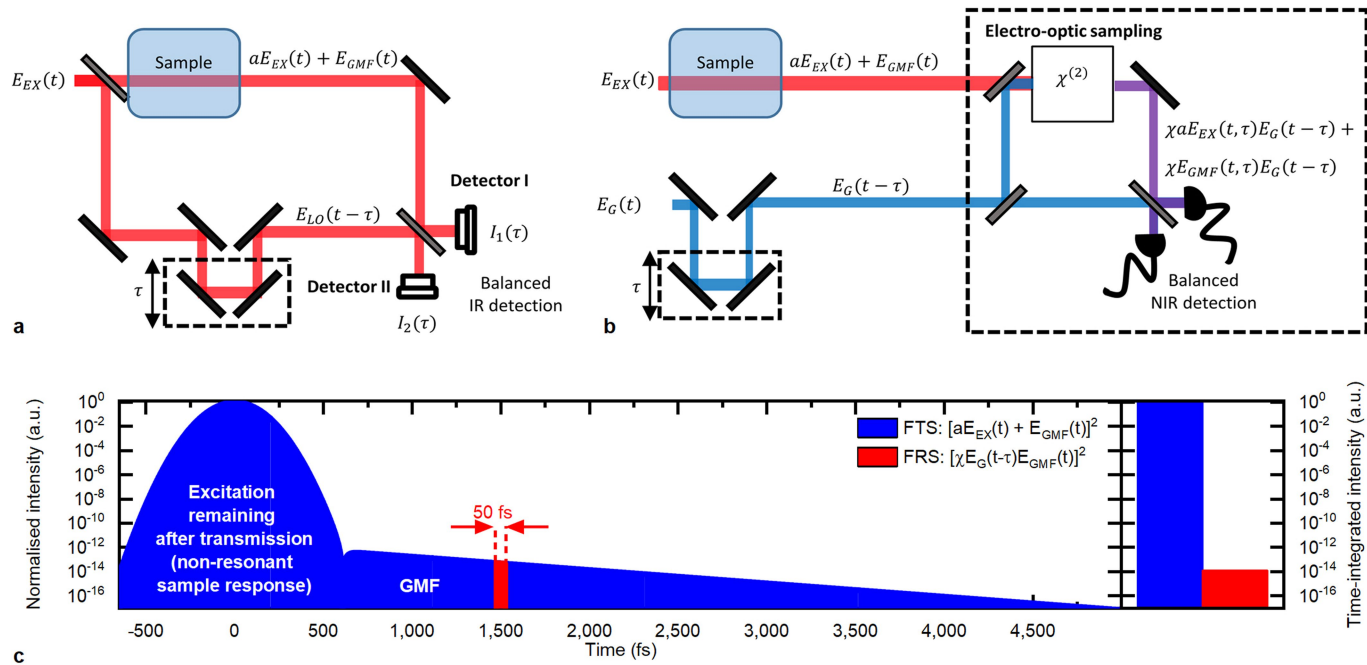
**Competing interests** The authors declare no competing interests.

### Additional information

**Supplementary information** is available for this paper at <https://doi.org/10.1038/s41586-019-1850-7>.

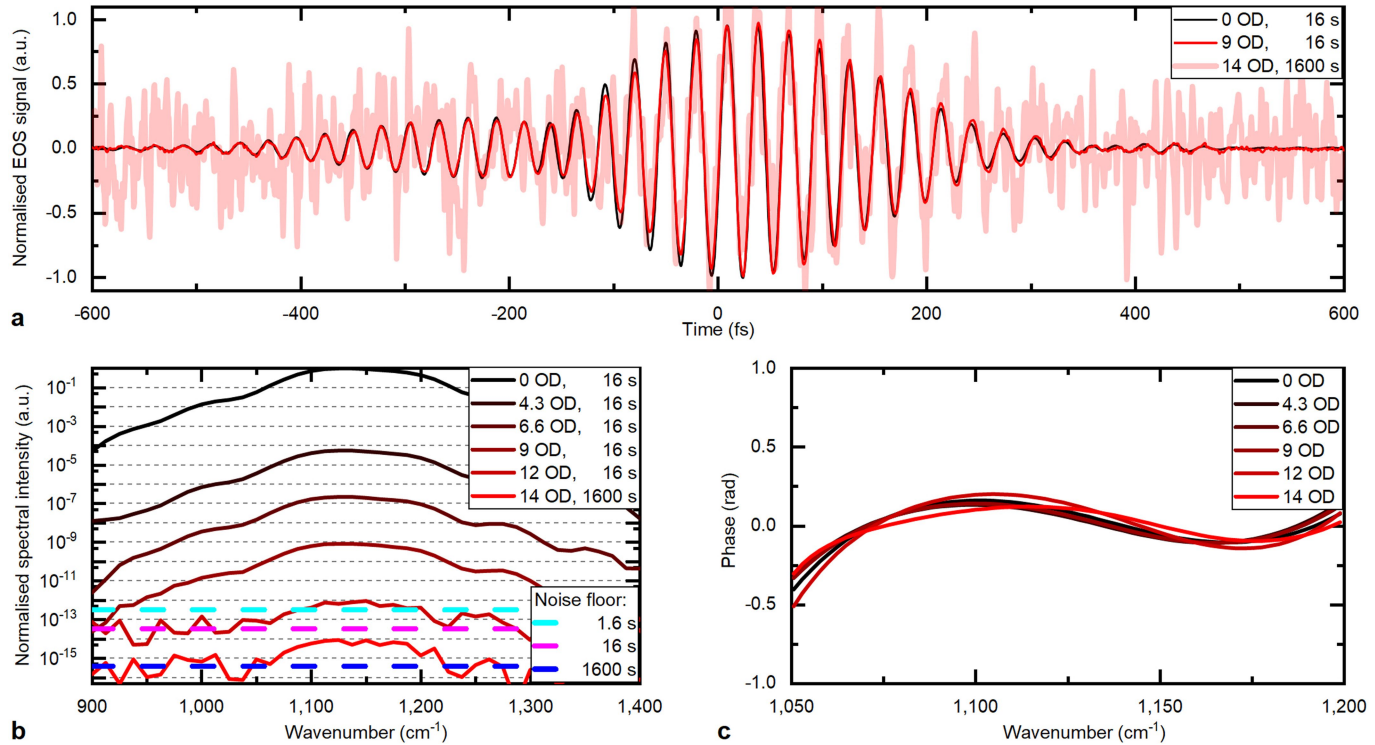
**Correspondence and requests for materials** should be addressed to I.P. or F.K.

**Reprints and permissions information** is available at <http://www.nature.com/reprints>.



**Extended Data Fig. 1 | Comparison of FTS with FRS. a**, Schematic of FTS. **b**, Schematic of FRS. **c**, Portions of the background signal contributed by the sample response to the FTS (blue, first right-hand-side term of equation (1a)) and to the FRS (red, first right-hand-side term of equation (1b)) signals at a fixed

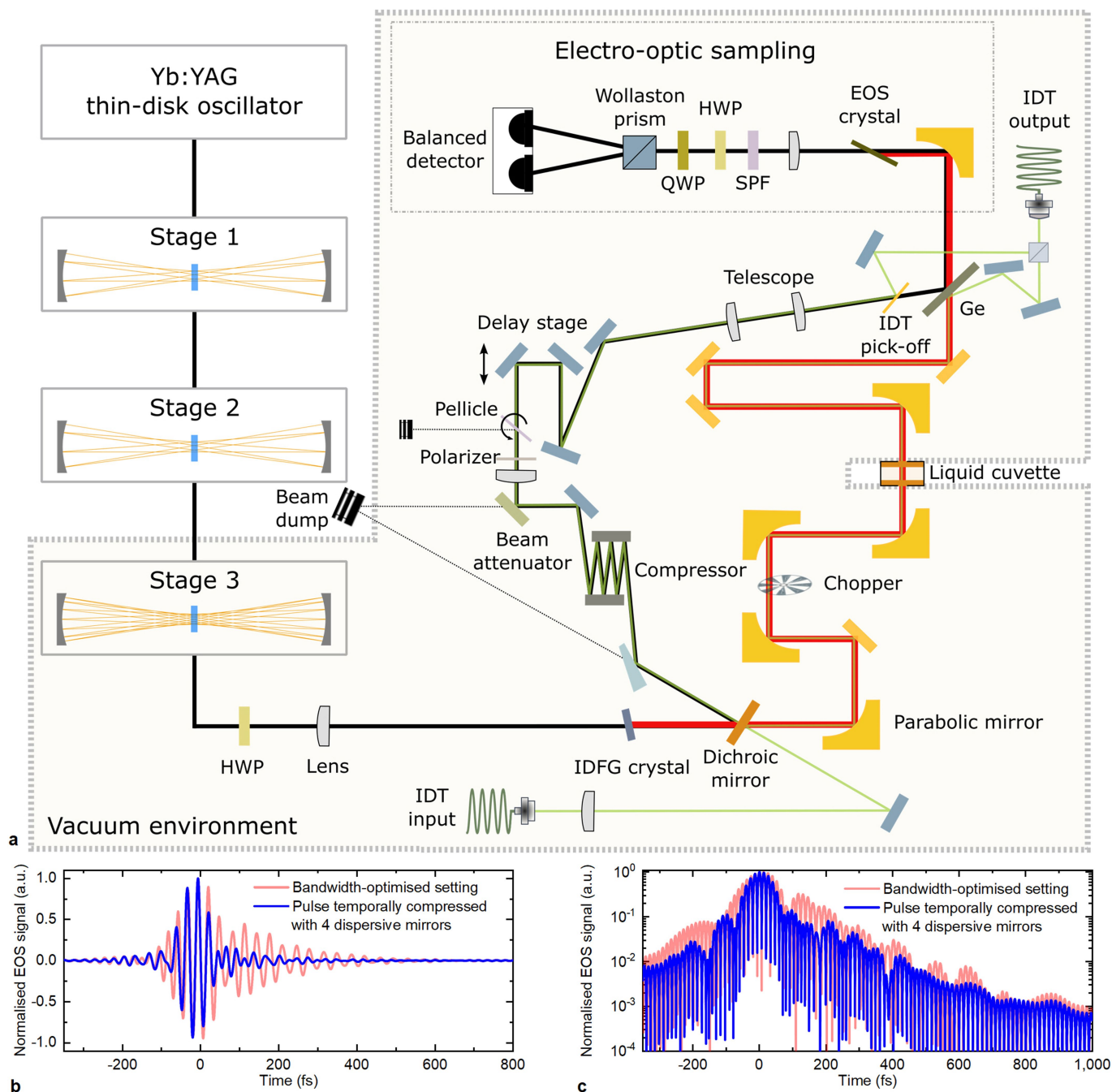
delay ( $\tau = 1,500$  fs). For illustration purposes, the nonlinear upconversion efficiency was set to 1 and the 'carved out' effective window time length to 50 fs (without loss of generality). Example parameters: 190-fs Gaussian excitation pulse and  $1,139\text{-cm}^{-1}$  DMSO<sub>2</sub> absorption (see Extended Data Table 1).



**Extended Data Fig. 2 | Detection dynamic range and linearity of the instrument response.**

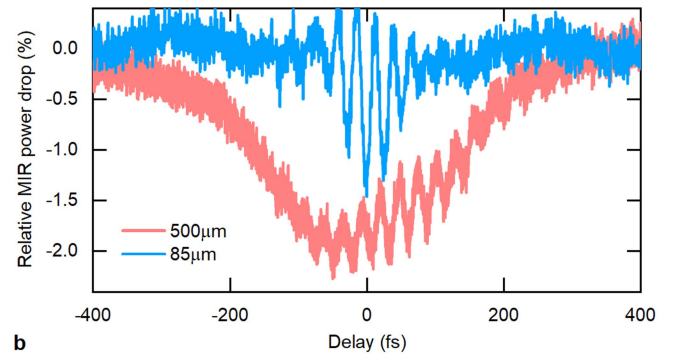
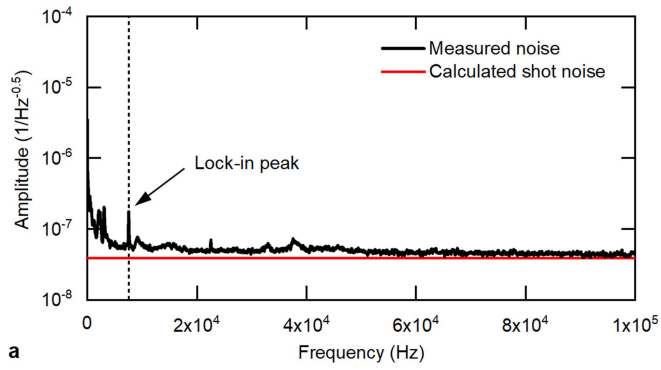
**a**, Infrared excitation pulse (normalized to maximum), recorded with attenuating optical density (OD) filters instead of the cuvette in the beam path, for increasing attenuation and measurement time  $T$ . A 1,200-fs scan range and  $T = 16$  s and  $T = 1,600$  s were considered. Small variations of the pulse shape for different attenuations are attributed to slight dispersion variations among the OD filters. The attenuation-independent pulse shape

confirms the instrument linearity over the entire parameter range considered. **b, c**, Spectral intensity (normalized to the maximum of the attenuation-free measurement) and phase of the signals in **a**, respectively. The detection noise floors in **b** were obtained by blocking the MIR signal and evaluating the mean of the (white) noise in the considered spectral range, and confirm the linear decrease of the noise floor with  $T$ . For the data in **c**, for all time-domain waveforms a super-Gaussian filter (width 700 fs, order 20) was applied.



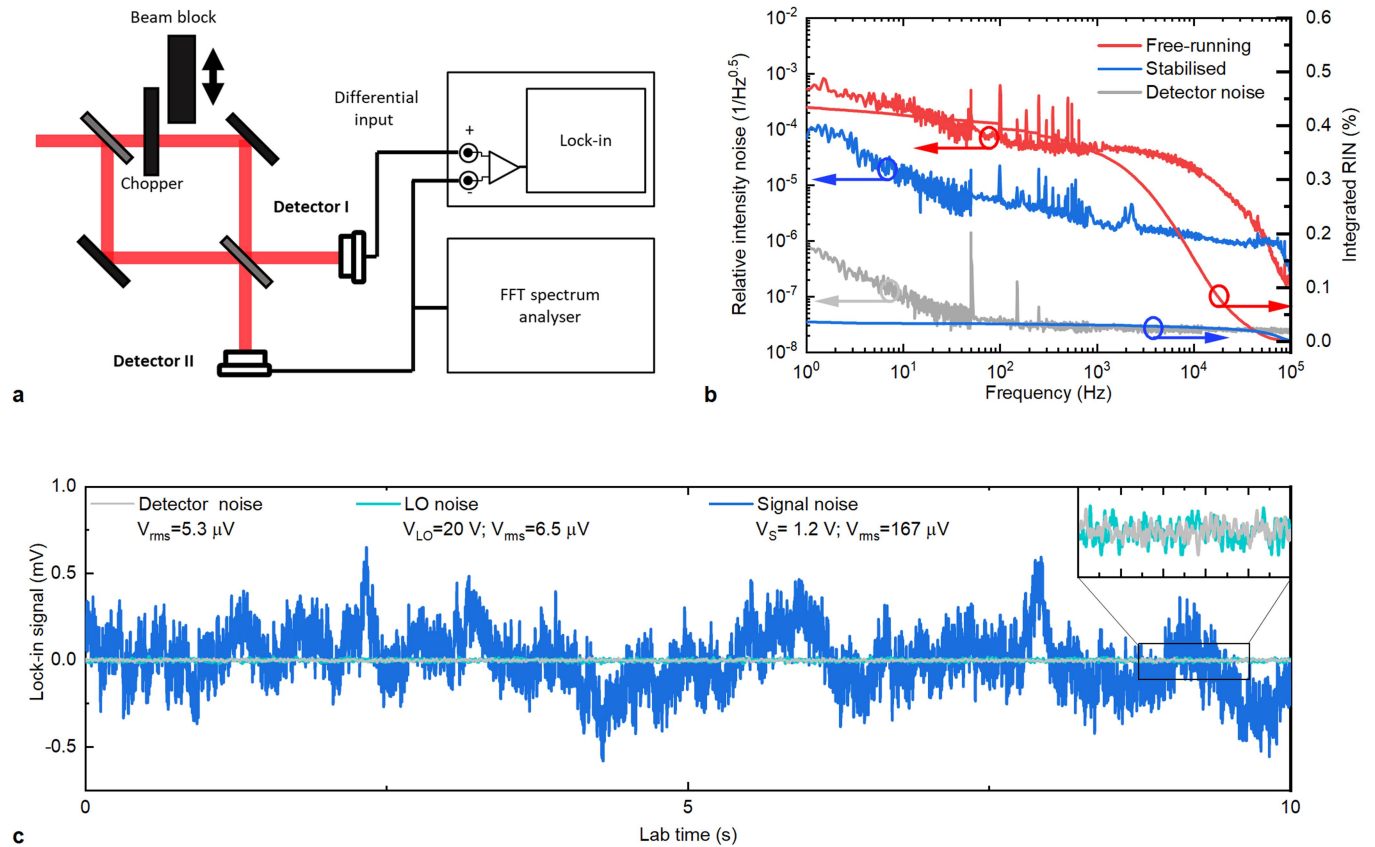
**Extended Data Fig. 3 | Experimental setup.** See subsection ‘High-power femtosecond oscillator and generation of waveform-stable MIR Pulses’ in Supplementary Information section I for details. **a**, HWP, half-wave plate; QWP, quarter-wave plate; IDFG, intra-pulse difference frequency generation; IDT, interferometric delay tracking; Ge, germanium beam combiner. All steering mirrors for the MIR beam were gold-coated. In the bandwidth-optimized instrument setting, four custom dispersive mirrors were added to the MIR

beam path (see text). The pulse was temporally compressed with customized dispersive optics. Pulse compression. EOS traces of the excitation pulse transmitted through water in the bandwidth-optimized instrument setting, with (blue) and without (red) four dispersive mirrors in the MIR beam path. **c**, As in **b** but on a logarithmic scale, visualizing the improved roll-off of the signal achieved with the dispersive optics.



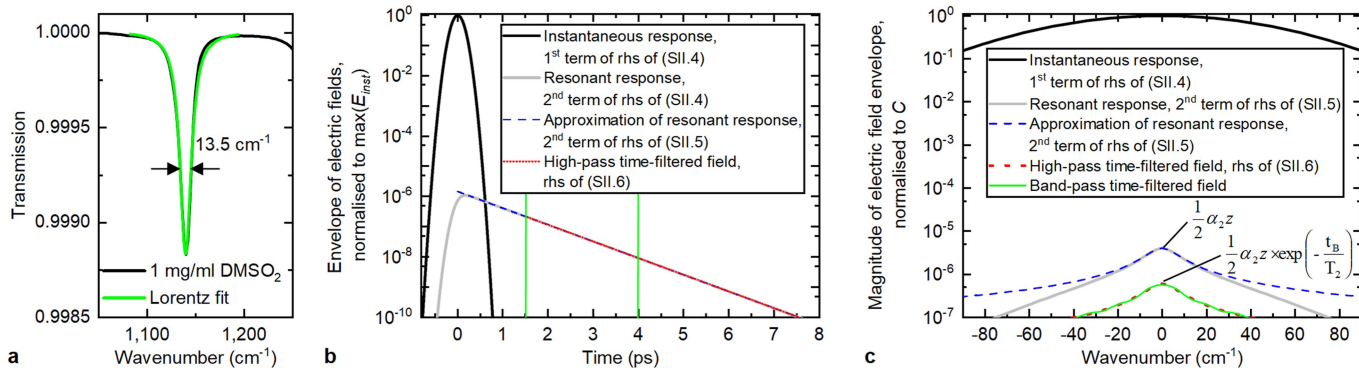
**Extended Data Fig. 4 | Contributions to quantum efficiency in electro-optic sampling.** **a**, Frequency-resolved measurement of the noise of the balanced detection (black), and calculated shot noise (red). The dashed line indicates the lock-in frequency, and its peak stems from the chopper. **b**, Comparison of MIR

power depletion after EOS crystal for the two different crystal thicknesses. The oscillations originate from interferences of the MIR pulse incident to the EOS crystal and MIR radiation generated therein (these oscillations do not affect the performance of EOS detection).



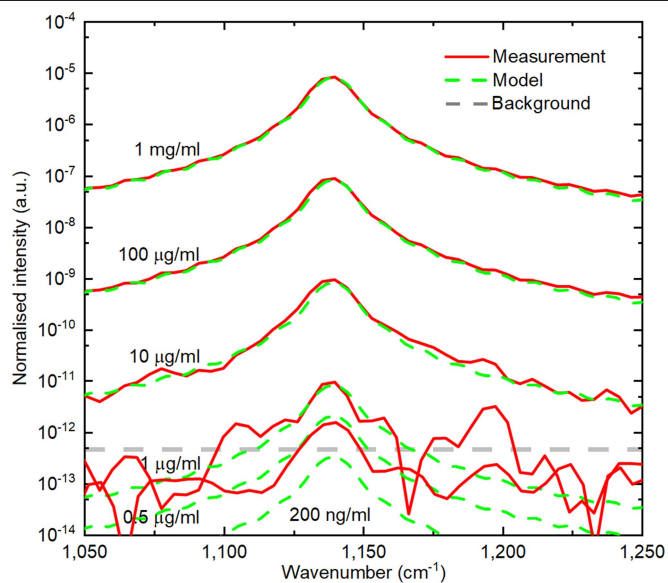
**Extended Data Fig. 5 | Measurement of noise contributions for the estimation of the performance of FTS with our femtosecond-laser-based source, our mechanical scan, and state-of-the-art infrared detection.** **a**, The setup mimics a FTS setup in the Mach-Zehnder configuration, with balanced lock-in detection. For lock-in frequency modulation, a mechanical chopper is placed in the ‘sample arm’. The two arms are recombined with a 50:50 beam splitter. The two outputs are detected with two independent MIR detectors (see text for details). The power impinging on each detector was limited to 450 mW, corresponding to a detector output voltage of 20 V. The relative intensity noise (RIN) spectrum of the source is recorded with an FFT-Analyser in the range 0.1–100 kHz (before balanced detection). Balanced lock-in

detection is performed with a lock-in amplifier with differential input. The beam block was used in the measurements shown in **c**. **b**, RIN spectrum of the free-running (red curve) and intensity-stabilized (blue curve) MIR beam (before the interferometer). The integrated RIN of the stabilized source from 1 Hz and 100 kHz is as low as 0.04%. **c**, Demodulated (after lock-in detection with a time constant of 1.6 ms and 4th-order filter) time-domain trace of detector noise (grey), local-oscillator signal with sample arm blocked (turquoise) and of the combination of both interferometer arms impinging on the balanced detection (blue). The inset shows a 1-second section of the signals, for a detailed comparison of the local-oscillator noise and the detector noise.

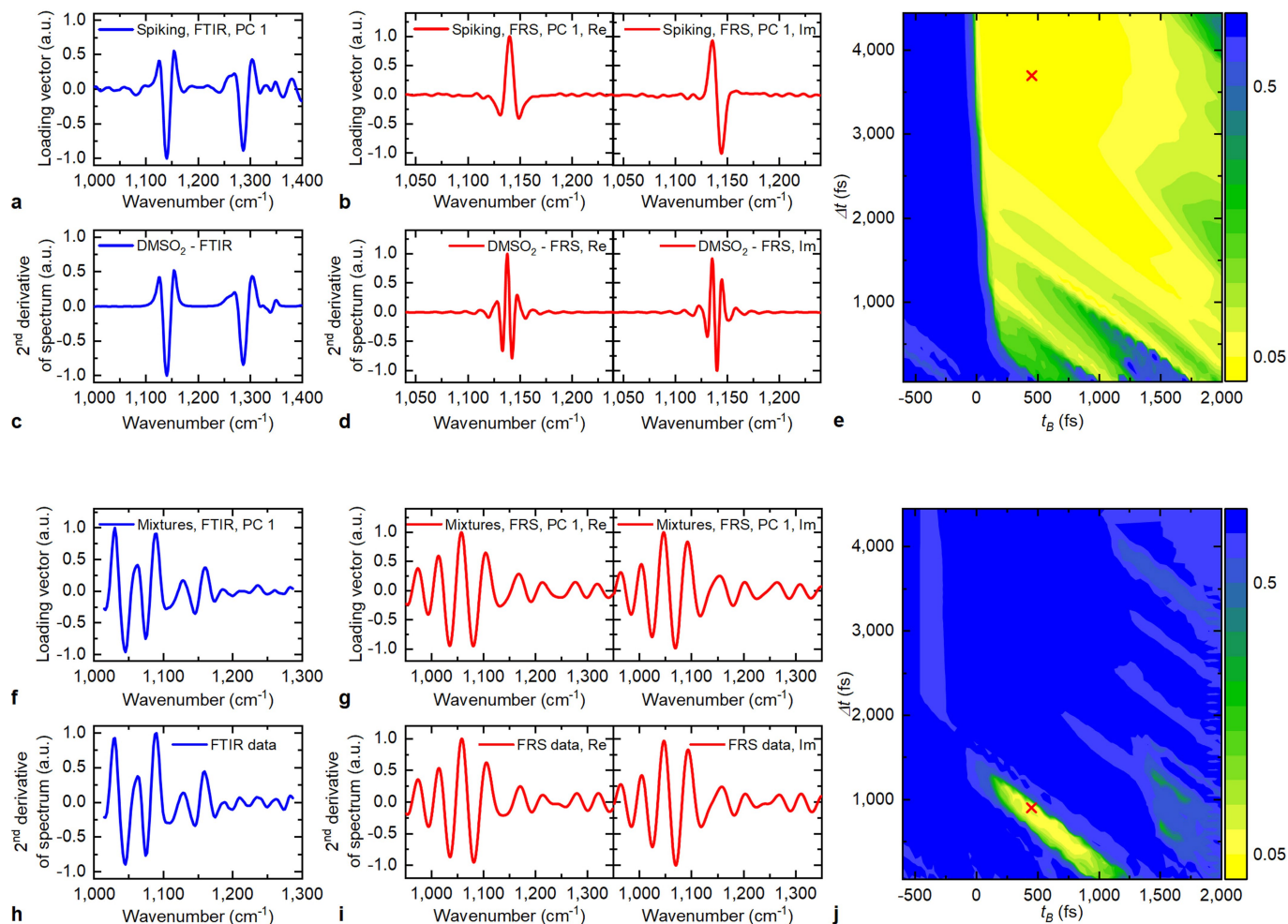


**Extended Data Fig. 6 | Simulations of time-domain decay of a molecular Lorentzian oscillator.** **a**, Fit of a Lorentzian oscillator to the  $1,139 \text{ cm}^{-1}$  absorption of (low-concentration) DMSO<sub>2</sub>. Black line, intensity transmission through pure, molecular DMSO<sub>2</sub>, determined by referencing the transmission spectrum of a  $1 \text{ mg ml}^{-1}$  solution to that of water, measured via FTIR, and normalizing to a  $1\text{-}\mu\text{m}$  path. Green line, least-squares fit ( $1,080\text{--}1,190 \text{ cm}^{-1}$ ) of a Lorentzian oscillator to the  $1,139 \text{ cm}^{-1}$  absorption, yielding a full width at half depth of  $13.47 \text{ cm}^{-1}$  and an absorption coefficient  $\alpha = 11.96 \text{ cm}^{-1}$ . The numerical example shows the instantaneous and resonant parts of the electric field as described by equations (1) to (4) in Supplementary Information section II. The initial pulse is a Gaussian pulse with an intensity envelope (full width at half maximum) of 190 fs. The Lorentzian absorption band has a peak of  $\alpha_2 z$  with  $\alpha_2 = 0.0024 \text{ cm}^{-1}$ , corresponding to a  $200 \text{ ng ml}^{-1}$  solution of DMSO<sub>2</sub> in water, and a width  $\delta\nu = 13.47 \text{ cm}^{-1}$ . These values were obtained from fitting a

Lorentzian absorber to the  $1,139 \text{ cm}^{-1}$  band of the transmission spectrum of a  $1 \text{ mg ml}^{-1}$  solution obtained with FTIR and linear extrapolation to a concentration 5,000 times lower. **b**, Time-domain representation of the normalized envelope functions of the electric fields described (see key). A value of  $t_B = 1.5 \text{ ps}$  is chosen. The green vertical bars indicate the boundaries of the band-pass-filtered resonant response shown in green: 1.5 ps and 4 ps. **c**, Magnitudes of the Fourier transforms of the envelopes shown in **a**, normalized to **C**. At the absorption maximum, the discrepancy between the resonant response as in Supplementary Information section 2 and its approximation as in Supplementary Information section 3 is 1%, justifying this convenient approximation. The error introduced by band-pass filtering the resonant response between 1.5 ps and 4 ps compared to the high-pass time-filtered signal is 4%.

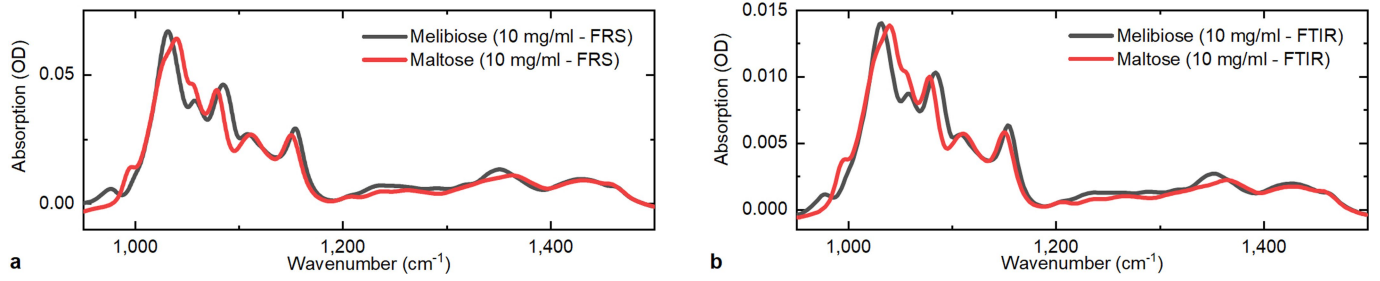


**Extended Data Fig. 7 | Spectral intensity of the Fourier-transformed temporal fingerprints of DMSO<sub>2</sub>.** Spectral intensity is shown for different concentrations, after high-pass-time-filtering at  $t_b = 1,500$  fs and subtraction of pure water reference, normalized to the spectral intensity of the reference pulse. Green dashed lines, modelled Lorentzian oscillator with the parameters derived from the fit in Extended Data Fig. 6. This model agrees excellently with the measured fingerprints, and confirms the minimum detectable absorbance predicted by equation (2) as well as the linear response of the instrument.



**Extended Data Fig. 8 | Principal component analysis.** **a–d**, Comparison of the loading vectors for the first principal component for the FTIR data (**a**) and the FRS data (**b**) from the serum spiking experiment, with the pre-processed GMF data (see text) of the FTIR (**c**) and FRS (**d**) measurements of a  $1 \text{ mg ml}^{-1}$  DMSO<sub>2</sub> solution. We note that the FRS spectra are complex, so the real and imaginary parts were considered separately (and stitched to single vectors). **e**, Figure of merit (FOM) (colour scale in arbitrary units; see Supplementary Information section VI) quantifying the separation of classes according to the first principal component (the lower the FOM, the better the separation), evaluated for a large

range of the beginning time  $t_B$  and time window length  $\Delta t$ . The cross indicates parameters yielding optimum separation. **f–i**, Comparison of the loading vectors for the first principal component for the FTIR data (**f**) and the FRS data (**g**) from the sugar mixture experiment, with the pre-processed GMF data of the FTIR (**h**) and FRS (**i**). For the latter, the difference of the spectra of the 50/50 mixture and the pure maltose solution is shown. The real and imaginary parts were considered separately. **j**, FOM quantifying the separation of classes according to the first principal component, in analogy to **e**.



**Extended Data Fig. 9 | Absorption spectra of 10 mg ml<sup>-1</sup> aqueous solutions of maltose and melibiose, measured by FRS and FTIR.** The difference in total absorption is due to the differing cuvette thickness. **a**, FRS; **b**, FTIR. OD, optical density.

**Extended Data Table 1 | Parameters for numerical estimation of the sensitivity of FTS implemented with our infrared source**

Parameter	Quantity	Comment
Central wavelength	$\lambda_C = 8.5 \mu m$	
Spectral width	$\Delta\nu_{FWHM} = 180 \text{ cm}^{-1}$	
MIR power (FTS)	$P_{LO} = P_S = 0.45 \text{ mW}$	Maximum incident power limited by detector saturation
MIR detector noise	$NEP_{MCT} = 2.5 \text{ pW/Hz}^{0.5}$	e.g.: InfraRed Associates; MCT-13-1.00
Relative intensity noise	$RIN = 2.7 \times 10^5 \text{ 1/Hz}^{0.5}$	
FTS detector efficiency	$\eta_{FTS} = 1$	Quantum efficiency is not stated in the detector datasheet
Measurement time	$T = 37 \text{ s}$	Measurement time for sample and reference measurement
Spectral resolution	$\nu_{res} = 4.7 \text{ cm}^{-1}$	This corresponds to a scan time window of 7 ps
<b>DMSO<sub>2</sub> absorption line at <math>\nu_{DMSO_2} = 1139 \text{ cm}^{-1}</math></b>		
Absorptivity	$\alpha_{DMSO_2} = 12.92 \text{ cm}^{-1}$	For 1 mg/ml DMSO <sub>2</sub> solution
Line width	$\nu_{FWHM} = 13.47 \text{ cm}^{-1}$	This corresponds to a dephasing time $T_2$ of ~770 fs